

corresponding to the Fourier transform of the kernel

$$\tilde{G}(y) = \text{sinc}\left(\frac{W_k y}{2s^2}\right) \quad (6)$$

where

$$s = \sqrt{\frac{\lambda_0 L_g}{\pi^2 \sqrt{\epsilon_c/\epsilon_0}}} \quad (7)$$

is a GRIN scale factor defined in (24). For such a transfer function, the required constitutive parameters are

$$\begin{aligned} \frac{\epsilon_{\text{ms}}(y)}{\epsilon_0} &= \frac{\mu_{\text{ms}}(y)}{\mu_0} \\ &= i \left(\frac{\lambda_0}{2\pi\Delta} \right) \ln \left[\frac{1}{\text{sinc}(W_k y/2s^2)} \right] \end{aligned} \quad (8)$$

The results of our simulation are shown in Fig. 2G, demonstrating good agreement with the analytical results.

In our second (GF) approach, we design a multilayered metamaterial slab, transversely homogeneous but longitudinally inhomogeneous, that realizes an output field distribution $g(y)$ to an input function $f(y)$, consistent with the GF $G(y)$ associated with a desired operator of choice (Fig. 3A). In this approach, we avoid the need of going into the Fourier domain, hence avoiding the GRIN subblocks that perform Fourier and inverse Fourier transforms. Because this GF slab is transversely symmetric, it can in principle realize an arbitrary GF with even symmetry, such as the second spatial derivative $g(y) \propto d^2 f(y)/dy^2$, which can be written in terms of an even kernel as $g(y) \propto \int f(u) \delta''(y-u) du$ [where the required GF is proportional to the second spatial derivative of the Dirac delta function $\delta''(y)$]. Our goal is then to tailor the transmission coefficient for impinging plane waves as a function of the transverse wavenumber k_y to be $\tilde{G}(k_y) \propto -k_y^2$. In (29), we addressed this problem within the framework of nonlocal transformation optics, assuming infinite media. Here, we consider a finite longitudinal thickness divided into N parallel layers with subwavelength thicknesses d_i , $i = 1, 2, \dots, N$ (Fig. 3A). We developed a fast synthesis approach to obtain the permittivity, permeability, and thickness of each layer required to tailor the overall plane-wave transmission coefficient to match $\tilde{G}(k_y)$ for all impinging angles (28). It is also possible to obtain the same result using nonmagnetic layered metamaterials by suitably increasing the number of layers, arguably simplifying the design and bringing it closer to practical realization. The 10-layered design (28) in Fig. 3B is a GF slab with nonmagnetic ($\mu = \mu_0$) constitutive parameters and an overall thickness comparable to λ_0 .

Our numerical results confirm that the designed metamaterial provides a GF kernel that resembles, given the unavoidable limited resolution, the desired $\delta''(y)$ at the output plane when the input is an approximate delta function. In Fig. 3, B and C, we apply a set of quadratic poly-

nomial functions and the Austin city skyline borders, respectively, as inputs for our second-spatial-derivative GF slab, showing the evolution of the z -component of the magnetic field distribution along the slab, and demonstrating that the designed structure indeed approximately performs the second-derivative operation as the wave propagates through it. Edge-detection spatial analog filters [e.g., Laplace filters (30)] and image-processing devices may largely benefit from this system. We also design a five-layered GF slab (with overall thickness of $0.37\lambda_0$) that performs the convolution operation of an input function with a one-wavelength rectangular spatial kernel (28). Figure 3D shows the simulation results using another rectangular function as input.

Our proposed computational metastructures are smaller than conventional lens-based optical signal-processing systems by several orders of magnitude. Moreover, with no analog-to-digital conversion or other systematic delays, here mathematical operations get processed as the electromagnetic signals propagate through the highly miniaturized and compact computational metamaterials. Such designs may potentially lead to direct, ultrafast, wave-based analog computation, equation solving, and signal processing at the hardware level.

References and Notes

1. N. Engheta, R. W. Ziolkowski, Eds., *Metamaterials—Physics and Engineering Explorations* (IEEE-Wiley, New York, 2006).
2. G. V. Eleftheriades, K. G. Balmann, *Negative-Refractive Metamaterials* (IEEE, New York, 2005).
3. D. R. Smith, J. B. Pendry, M. C. K. Wiltshire, *Science* **305**, 788–792 (2004).
4. C. Caloz, T. Itoh, *Electromagnetic Metamaterials—Transmission Line Theory and Microwave Applications* (IEEE-Wiley, New York, 2006).
5. W. Cai, V. Shalaev, *Optical Metamaterials: Fundamentals and Applications* (Springer, New York, 2010).
6. J. B. Pendry, D. Schurig, D. R. Smith, *Science* **312**, 1780–1782 (2006).
7. U. Leonhardt, *Science* **312**, 1777–1780 (2006).

8. A. Alù, N. Engheta, *Phys. Rev. E* **72**, 016623 (2005).
9. A. Vakil, N. Engheta, *Science* **332**, 1291–1294 (2011).
10. E. F. Kuester, M. A. Mohamed, M. Piket-May, C. L. Holloway, *IEEE Trans. Antenn. Propag.* **51**, 2641–2651 (2003).
11. N. Yu et al., *Science* **334**, 333–337 (2011).
12. X. Ni, N. K. Emani, A. V. Kildishev, A. Boltasseva, V. M. Shalaev, *Science* **335**, 427 (2012).
13. Y. Zhao, M. A. Belkin, A. Alù, *Nat. Commun.* **3**, 870 (2012).
14. A. Pandey, N. M. Litchinitser, *Opt. Lett.* **37**, 5238–5240 (2012).
15. Y. Lai et al., *Phys. Rev. Lett.* **102**, 253902 (2009).
16. D. de Solla Price, *IEEE Micro.* **4**, 22–52 (1984).
17. A. B. Clymer, *IEEE Ann. Hist. Comput.* **15**, 19 (1993).
18. Computer History Museum, www.computerhistory.org/revolution/analog-computers/3.
19. G. W. Milton, *J. Mech. Phys. Solids* **61**, 1543–1560 (2013).
20. A. B. Kempe, *Proc. London Math. Soc.* **7**, 213 (1876).
21. A. Weiner, *Rev. Sci. Instrum.* **71**, 1929 (2000).
22. D. Casasent, *Proc. IEEE* **65**, 143–157 (1977).
23. J. Goodman, *Introduction to Fourier Optics* (Roberts & Co., Englewood, CO, ed. 3, 2005).
24. H. M. Ozaktas, D. Mendlovic, *J. Opt. Soc. Am. A* **10**, 2522 (1993).
25. J. B. Pendry, S. A. Ramakrishna, *J. Phys. Condens. Matter* **15**, 6345–6364 (2003).
26. G. V. Naik, J. Kim, A. Boltasseva, *Opt. Mater. Express* **1**, 1090 (2011).
27. F. Monticone, N. M. Estakhri, A. Alù, *Phys. Rev. Lett.* **110**, 203903 (2013).
28. See supplementary materials on Science Online.
29. G. Castaldi, V. Galdi, A. Alù, N. Engheta, *Phys. Rev. Lett.* **108**, 063902 (2012).
30. R. C. Gonzalez, R. E. Woods, *Digital Image Processing* (Prentice Hall, New York, 2008).

Acknowledgments: Supported in part by U.S. Office of Naval Research Multidisciplinary University Research Initiative (MURI) grant N00014-10-1-0942.

Supplementary Materials

www.sciencemag.org/content/343/6167/160/suppl/DC1
Materials and Methods
Supplementary Text
Figs. S1 to S23
Tables S1 and S2
References (31–35)

5 July 2013; accepted 12 November 2013
10.1126/science.1242818

Heteroepitaxial Growth of Two-Dimensional Hexagonal Boron Nitride Templated by Graphene Edges

Lei Liu,^{1*} Jewook Park,^{2*} David A. Siegel,³ Kevin F. McCarty,³ Kendal W. Clark,² Wan Deng,¹ Leonardo Basile,^{2,4} Juan Carlos Idrobo,² An-Ping Li,^{2†} Gong Gu^{1†}

By adapting the concept of epitaxy to two-dimensional space, we show the growth of a single-atomic-layer, in-plane heterostructure of a prototypical material system—graphene and hexagonal boron nitride (h-BN). Monolayer crystalline h-BN grew from fresh edges of monolayer graphene with atomic lattice coherence, forming an abrupt one-dimensional interface, or boundary. More important, the h-BN lattice orientation is solely determined by the graphene, forgoing configurations favored by the supporting copper substrate.

In conventional heteroepitaxial growth, an extended single-crystal film, or epilayer, forms on a two-dimensional (2D) surface of a single crystal of a different material, as exemplified by

the growth of GaAs on Si (*1*). In general, if the lattice constants of the different materials are similar, the atomic lattice of the surface can act as a template for the initial growth of the

epilayer and ensure that it forms a single crystal. Because of the interactions in 3D space between the 2D seed crystal and the surroundings, it is not a trivial question whether a purely 2D heteroepitaxial crystal would grow from the 1D edge of a 2D seed crystal, with the crystallography of the epitaxial crystal solely determined by the seed. Here, we implement heteroepitaxy in a 2D material system by growing monolayer hexagonal boron nitride (h-BN; BN hereafter) from the edges of existing graphene crystals, which have a close lattice match (1.7%). We demonstrate abrupt zigzag boundaries as well as lattice coherence between the graphene “substrate” and the BN “epilayer.”

The growth method is schematically illustrated in Fig. 1A and described in detail in the supplementary materials (2). First, monolayer graphene single crystals (fig. S1) were grown by atmospheric-pressure chemical vapor deposition (APCVD) (3, 4) on a Cu foil, providing the substrate in 2D space. Immediately before BN growth, we performed a hydrogen etch (4–6) to obtain fresh edges, or “surfaces” in 2D. Graphene island edges were etched back, and equiangular hexagon etch holes with zigzag edge sides (5) formed, which exhibited distinctive 120° angles, as revealed by scanning electron microscopy (SEM) (Fig. 1B). This step is analogous to the common practice of obtaining fresh starting surfaces for conventional epitaxy and is critical to the formation of the BN epilayer here. For controlled BN epilayer formation, we ensure that (i) the growth is indeed confined in a 2D space—the Cu surface—and (ii) the growth is sufficiently slow to allow for epitaxial growth. A low precursor ($\text{BH}_3\text{--NH}_3$) supply rate satisfies both requirements and was achieved with APCVD exploiting process kinetics (7), analogous to graphene APCVD using highly diluted CH_4 precursor that yields crystallites with zigzag edges (3, 4).

The early stage of BN-“on”-graphene heteroepitaxy in 2D shown in Fig. 1C revealed several BN islands, with a distinct contrast in the SEM image, forming at the graphene edges. Figure 1D shows the formation of BN epilayers in 2D, which we refer to as “epistrips.” The growth of the epistrip, which is a 2D crystal, is different from seeded lateral epitaxy (8) of 3D crystalline films. Figure 1E shows graphene islands enclosed by continuous epistrips. Eventually, all etch holes in graphene were filled by BN (Fig. 1F). No second-layer formation was observed in SEM. Atomic resolution scanning tunneling microscopy (STM) revealed atomic-level details of graphene-BN boundaries (2), with the assignment of graphene and BN regions made by their

distinctive scanning tunneling spectra (STS), as discussed in detail below. Figure 1G shows an abrupt boundary as well as lattice coherence between graphene and BN. Electron diffraction experiments to be discussed below confirm lattice coherence on larger length scales and, more important, show that the BN epistrip crystalline orientation is solely determined by the graphene seed, independent of the underlying Cu lattice.

These results differ fundamentally from those of the previous demonstrations of graphene-BN heterostructure growth. In-plane graphene-BN heterostructures were demonstrated (9, 10) on Cu foils by top-down patterning and regrowth, without or agnostic of graphene-BN lattice coherence, which is unnecessary for the intended ultrathin circuit board or passive component applications. Also, on polycrystalline Cu foils by chemical vapor deposition (CVD), a variety of hybrid vertical/in-plane heterostructures were synthesized (11). On single-crystal metal substrates in ultrahigh vacuum chambers, two-step growth methods resulted in patchworks of graphene and BN domains, which exhibited lattice coherence that is coincident with epitaxy in the third dimension because the graphene and the BN are both epitaxial to the single-crystal supporting substrates (12, 13). This coincidence masks possible heteroepitaxy in 2D, especially for the case (13) where BN nucleated at graphene edges.

We examined the heterostructure by STM after annealing the Cu foil sample in the STM system at 430°C for 48 hours to relax strain (14). The 2D heterostructure did not need to be transferred from the Cu foil, thus avoiding transfer-induced contamination (2). The STM image in Fig. 2A shows the seamless connection between lower graphene and higher BN regions, which have an apparent height difference. Although electronic properties contribute to apparent heights, the observed difference is considerably smaller than the interlayer spacings of graphene (3.37 Å) and BN (3.33 Å) (15), confirming the in-plane connection between graphene and BN and the absence of additional layers. Notably, each segment of the boundary is zigzag oriented, consistent with the formation of zigzag graphene edges by the hydrogen etch (4, 5). Furthermore, enlarged images (fig. S3, B and C) of the graphene and BN regions in fig. S3A, along with their 2D fast Fourier transforms (insets to figs. S2, B and C), show no discernible rotational misalignment between the two, corroborated by Z-contrast scanning transmission electron microscopy (STEM) (fig. S10). The measured lattice constants of graphene (2.46 ± 0.04 Å) and BN (2.50 ± 0.04 Å) are consistent with reported values (2.46 Å and 2.50 Å) (15). Moreover, the STEM results also indicate that the interface boundary is formed by monolayer graphene and BN (fig. S11A) and that it is sharp, with a transition width of ~ 0.5 nm (fig. S11B).

Graphene and BN regions can be identified by simultaneously acquiring STM images and STS. Differential tunneling conductance (dI/dV) maps (Fig. 2B and fig. S3F) clearly show two

distinct regions, with segments of the boundary forming distinctive 120° angles. To elucidate the assignment of graphene and BN regions, we show in Fig. 2D a series of STS curves obtained along a line across a boundary. Figure 2C marks the location where each curve was obtained. The top curves (yellow, magenta, and cyan) are characteristic of graphene (16), with the Dirac point ~ 300 mV below the Fermi level. The black curve displays metallic behavior, which we attribute to an interface band between BN and Cu, following the analysis of Joshi *et al.*, who considered the BN transparent at these low biases (17). Noticeably, the zero-bias differential conductance was lower in the BN region. Thus, in the dI/dV map obtained at a low sample bias $V = 0.1$ V shown in fig. S3F, we assigned the low differential conductance region to BN. At a high bias $V = 1$ V, the differential conductance map is reversed (Fig. 2B).

To show lattice coherence between the graphene substrate and the BN epistrip over larger length scales than atomic-resolution images and, more important, the overriding of the influence of the underlying Cu lattice, we investigated a sample by low-energy electron microscopy (LEEM) and micro low-energy electron diffraction (μ -LEED). Preserving the Cu support allowed us to study the heterostructure crystallography with regard to the underlying Cu surface, which consists predominantly of (100)-oriented grains (18). The LEEM image in Fig. 3A shows the graphene cores, the BN epistrips, and the bare Cu with bright, dim, and dark contrasts, respectively. The μ -LEED patterns acquired at eight locations are shown in Fig. 3, B to I (corresponding to locations labeled B to I in Fig. 3A). The four first-order diffraction spots arising from the Cu(100) surface [marked by blue circles with one connected to the (00) spot with a blue arrow] in all eight patterns show the same orientation, indicating that the imaged area is a single Cu grain. The graphene and BN spots are circled, with one connected to the (00) spot by an arrow, in red and green, respectively. Comparing diffraction patterns of the graphene cores and their corresponding BN epistrips, we notice that all BN epistrips are orientationally aligned to their graphene cores, regardless of the rotation angle between the graphene-BN lattice and the underlying Cu(100) surface lattice. The rotation is labeled for each LEED pattern. The top, middle, and bottom panels of Fig. 3J depict real-space structures corresponding to the three rotations, +16°, -6°, and 0°, respectively.

Whereas graphene does not align to the underlying Cu(100) at particular rotation angles (18), BN exhibits a definitive alignment when grown on a bare Cu foil (with 0° rotation; see the supplementary materials). Here, grown as the epistrip, or epilayer in 2D, the BN adopts the orientation of the graphene, because the in-plane interaction is much stronger than and thus overrides the out-of-plane interaction with the Cu. This observation is the best manifestation of epitaxy in 2D, in contrast to graphene-BN lattice coherence mediated by an underlying metal

¹The University of Tennessee, Knoxville, TN 37996, USA. ²Center for Nanophase Materials Sciences, Oak Ridge National Laboratory, Oak Ridge, TN 37831, USA. ³Sandia National Laboratories, Livermore, CA 94550, USA. ⁴Departamento de Física, Escuela Politécnica Nacional, Quito, Ecuador.

*These authors contributed equally to this work.

†Corresponding author. E-mail: ggu1@utk.edu (G.G.); apli@ornl.gov (A.-P.L.)

Fig. 1. Heteroepitaxy in 2D space. (A) Cartoon illustration of epitaxial growth of BN onto graphene edges. Black, blue, red, and small gray spheres visualize C, N, B, and H atoms, respectively. The reliance on the catalytic Cu surface for precursor ($\text{H}_3\text{B}-\text{NH}_3$) decomposition confines the growth to 2D. (B) SEM image of a hydrogen-etched graphene (Gr) island with equiangular hexagon etch holes. (C) Nucleation of BN at graphene edges during initial growth. (D) Formation of BN epistrips at graphene edges. (E) Continuous BN epistrips enclosing graphene islands. (F) Full coverage of the etch holes in a graphene island by BN. (G) Atomic-resolution STM image (3.5 nm by 2.5 nm) of a graphene-BN boundary. A honeycomb lattice and zigzag boundaries are overlaid on the image.

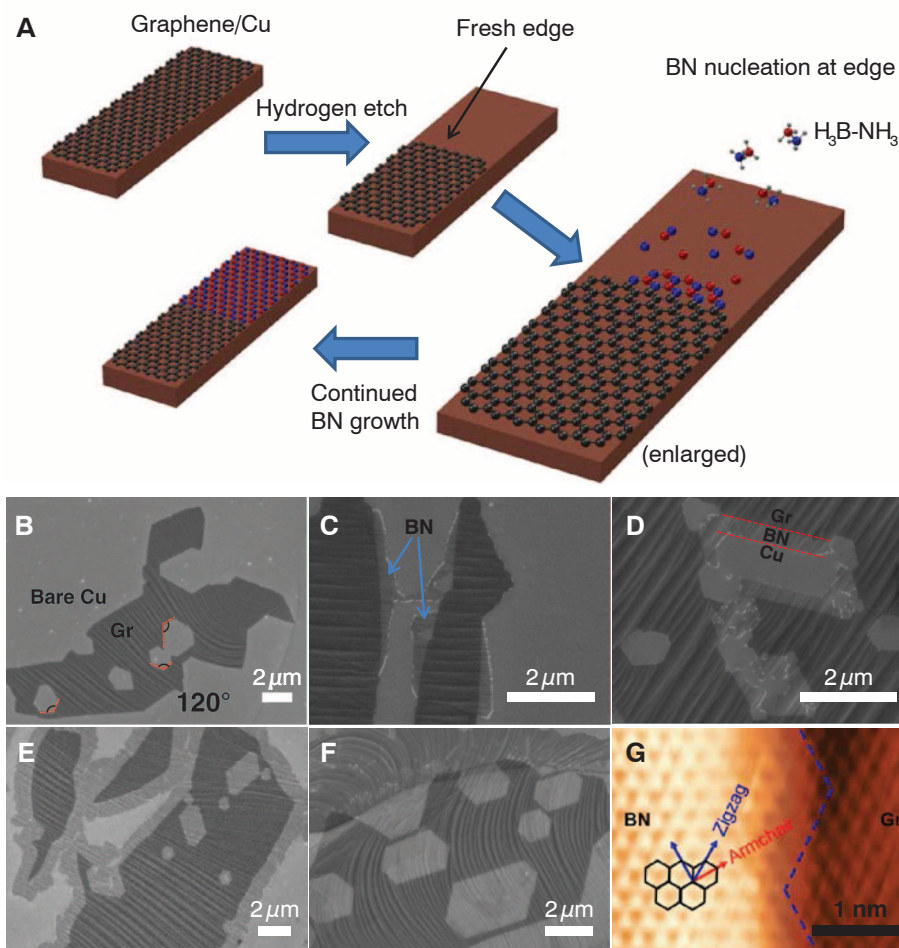
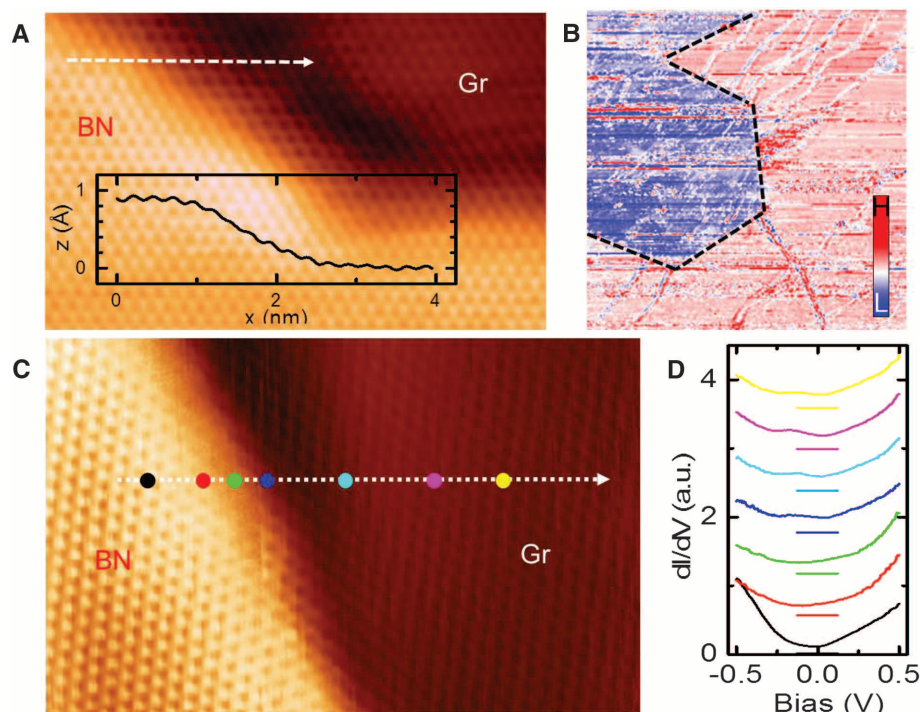


Fig. 2. Graphene-BN boundary structure at atomic scale. (A) STM image at a graphene-BN boundary (7.5 nm by 5 nm, sample bias 0.5 V). (Inset) Height profile along the white dashed arrow across the boundary. (B) Differential tunneling conductance map simultaneously obtained in the same region as fig. S3E (1 μm by 1 μm ; 1 V sample bias voltage; 200 pA tunneling current). (C) STM image (8 nm by 5 nm) of a graphene-BN boundary, with colored dots marking locations of STS acquisition. (D) dI/dV curves color coded by location and offset for clarity, with horizontal lines indicating zero differential conductance.



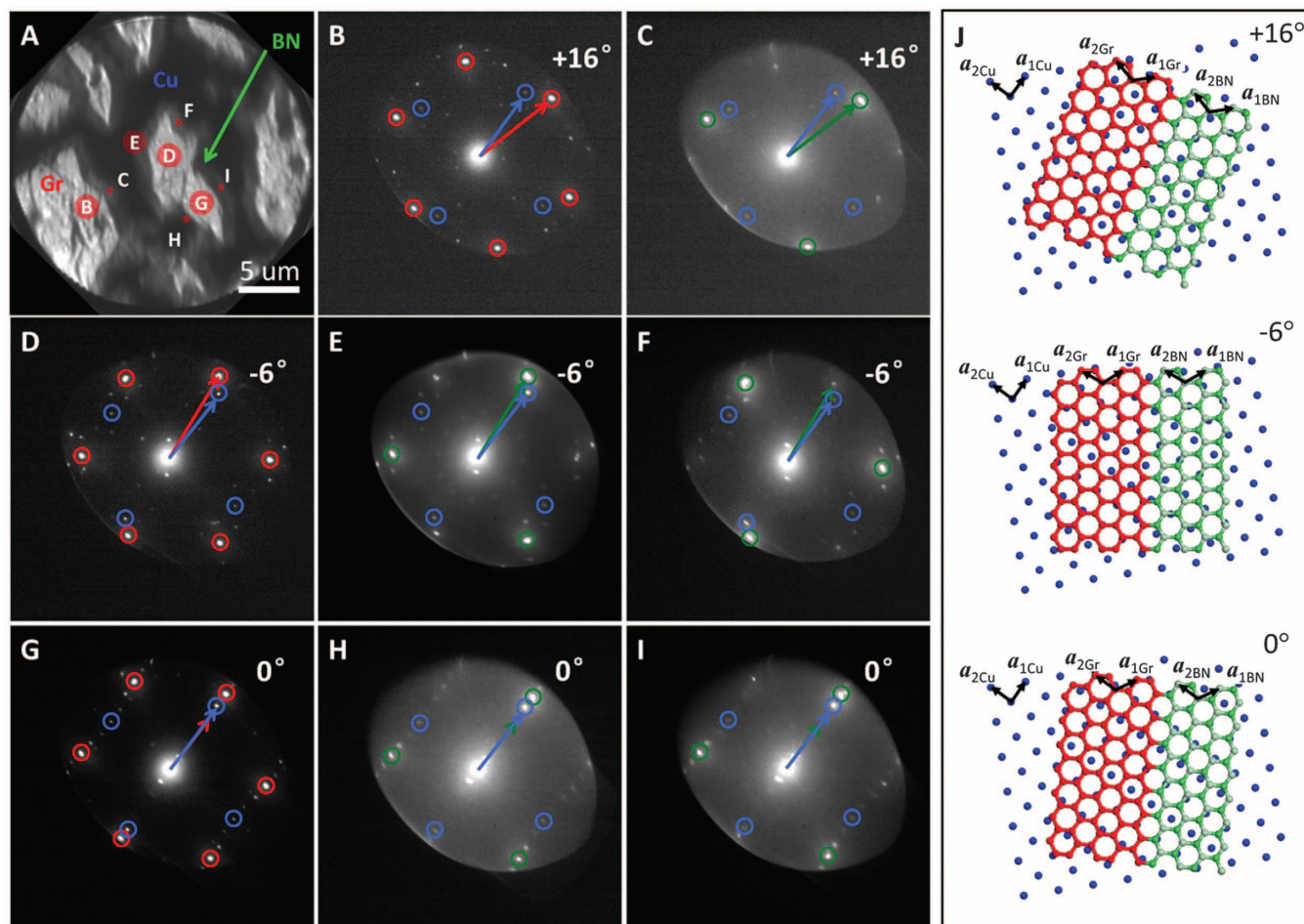


Fig. 3. Graphene-BN boundary structure at mesoscopic scale. (A) LEEM image of BN epistrips grown onto edges of graphene (Gr), the brightest regions. The darkest and the medium gray regions are bare Cu and BN, respectively. The labeled circles show the locations and sizes (0.5 or 2 μm diameter) of the regions analyzed in the μ -LEED patterns of (B) to (I). (B to I) LEED patterns acquired at locations marked in (A). The first-order diffraction spots and reciprocal lattice vectors of Cu, graphene, and BN are distinguished by

blue, red, and green colors, respectively. Each BN epistrip and the corresponding graphene substrate have the same in-plane orientation with respect to the underlying Cu lattice: rotations of $+16^\circ$ [(B) and (C)], -6° [(D) to (F)], and 0° [(G) to (I)]. (J) Real-space structure models corresponding to the three rotations. Following (B) to (I), blue, red, and green represent Cu, graphene, and BN, respectively; B and N atoms are symbolized by two shades of green. Lattice vectors are shown.

lattice (12, 13). The epistrip is purely 2D and is not necessarily epitaxial to the support in the third dimension. Thus, epitaxy in 2D is not to be confused with the Frank-van der Merwe film growth mode (sometimes referred to as 2D growth) (8).

As expected, the BN patterns exhibit three-fold symmetry, a feature besides LEEM contrast distinguishing it from the six-fold symmetric graphene. Interestingly, the BN spots in Fig. 3, E and F, acquired on BN epistrips of the same graphene core, are mirror images of each other, whereas those in Fig. 3, H and I, are the same. This observation relates to the well-known antiphase phenomenon in polar-on-nonpolar epitaxy (1) and has implications in the spin and magnetic properties of the boundaries (19, 20).

Now we discuss the rationale behind heteroepitaxy in 2D space. Although the growth of 2D crystals has been extensively studied (15, 21–25) and 2D heterostructures have been synthesized recently (9–13), it has until now been unclear whether a purely 2D heterostructure (criterion 1)

can form by the growth of an epistrip from the 1D edge of a seed 2D crystal (criterion 2) with the crystallography of the epistrip solely determined by the seed (criterion 3). Because of the complex interactions in 3D space that involve the 2D crystal, the supporting substrate, and the feed gas, the three criteria closely intertwine. To meet criterion 1, the supporting substrate must at the same time serve as a constraint that confines the growth process on its surface to avoid the formation of multiple stacked sheets. We achieved confinement by limiting the precursor feed rate, leveraging the catalytic property of Cu (2, 22, 23). Criterion 2 can be met if the supporting substrate surface is sufficiently uniform to suppress nucleation (which results from interactions between the supporting substrate and feed gas) away from the seed 2D crystal edge. Simultaneously meeting criteria 2 and 3 is subtle, however, because of the interaction between BN and the Cu support. In the absence of graphene seeds, BN definitively aligns with the underlying Cu lattice (2). In

contrast, graphene itself exhibits a wide distribution of orientations relative to the underlying Cu lattice (18). For intended heteroepitaxy in 2D, therefore, it is not obvious whether the BN epistrip will preferably nucleate at the graphene edge, adopting its orientation, or elsewhere aligning to the Cu lattice. This work demonstrates that, at least in one prototypical material system, the epistrips indeed nucleate at the seed crystal edge to form a 2D heterostructure. The growth of other 2D crystals, such as metal dichalcogenides (24, 25), has been established, providing the foundation to explore heteroepitaxy in 2D space based on those materials. There, the three criteria intertwine in different ways and need to be met by leveraging different mechanisms.

References and Notes

1. H. Kroemer, *J. Cryst. Growth* **81**, 193–204 (1987).
2. Supplementary materials are available on Science Online.
3. Q. Yu et al., *Nat. Mater.* **10**, 443–449 (2011).
4. I. Vlassiok et al., *ACS Nano* **5**, 6069–6076 (2011).

5. Y. Zhang, Z. Li, P. Kim, L. Zhang, C. Zhou, *ACS Nano* **6**, 126–132 (2012).
6. S. Choubak, M. Biron, P. L. Levesque, R. Martel, P. Desjardins, *J. Phys. Chem. Lett.* **4**, 1100–1103 (2013).
7. J. D. Plummer et al., *Silicon VLSI Technology: Fundamentals, Practices and Modeling* (Prentice Hall, Upper Saddle River, NJ, 2000).
8. M. Ohring, *Materials Science of Thin Films* (Academic Press, Waltham, MA, ed. 2, 2002).
9. M. P. Levendorf et al., *Nature* **488**, 627–632 (2012).
10. Z. Liu et al., *Nat. Nanotechnol.* **8**, 119–124 (2013).
11. S. M. Kim et al., *Nano Lett.* **13**, 933–941 (2013).
12. Y. B. Gao et al., *Nano Lett.* **13**, 3439–3443 (2013).
13. P. Sutter, R. Cortes, J. Lahiri, E. Sutter, *Nano Lett.* **12**, 4869–4874 (2012).
14. J. Tian et al., *Nano Lett.* **12**, 3893–3899 (2012).
15. C. Oshima, A. Nagashima, *J. Phys. Condens. Matter* **9**, 1–20 (1997).
16. Y. Zhang et al., *Nat. Phys.* **4**, 627–630 (2008).
17. S. Joshi et al., *Nano Lett.* **12**, 5821–5828 (2012).
18. J. M. Wofford, S. Nie, K. F. McCarty, N. C. Bartelt, O. D. Dubon, *Nano Lett.* **10**, 4890–4896 (2010).
19. J. M. Pruneda, *Phys. Rev. B* **81**, 161409 (2010).
20. S. Bhowmick, A. K. Singh, B. I. Yakobson, *J. Phys. Chem. C* **115**, 9889–9893 (2011).
21. J. Wintterlin, M.-L. Bocquet, *Surf. Sci.* **603**, 1841–1852 (2009).
22. X. Li et al., *Science* **324**, 1312–1314 (2009).
23. K. K. Kim et al., *Nano Lett.* **12**, 161–166 (2012).
24. S. Najmaei et al., *Nat. Mater.* **12**, 754–759 (2013).
25. A. M. van der Zande et al., *Nat. Mater.* **12**, 554–561 (2013).

Acknowledgments: This work was partially supported by NSF (ECCS-1231808), the Defense Advanced Research Projects Agency (approved for public release; distribution is unlimited), and the National Secretariat of Higher Education, Science, Technology and Innovation of Ecuador (SENESCYT). A portion

of this research was conducted at the Center for Nanophase Materials Sciences (CNMS), which is sponsored at Oak Ridge National Laboratory by the Scientific User Facilities Division, Office of Basic Energy Sciences, U.S. Department of Energy. Work at Sandia was supported by the Office of Basic Energy Sciences, Division of Materials and Engineering Sciences, U.S. Department of Energy, under contract DE-AC04-94AL85000. We thank R. M. Feenstra for discussions on LEEM. Authors declare no conflicts of interest.

Supplementary Materials

www.sciencemag.org/content/343/6167/163/suppl/DC1
Materials and Methods
Supplementary Text
Figs. S1 to S11
Reference (26)

18 September 2013; accepted 3 December 2013
10.1126/science.1246137

Self-Accelerating CO Sorption in a Soft Nanoporous Crystal

Hiroshi Sato,^{1,2} Wataru Kosaka,^{1,2} Ryotaro Matsuda,^{1,2*} Akihiro Hori,² Yuh Hijikata,³ Rodion V. Belosludov,⁴ Shigeyoshi Sakaki,³ Masaki Takata,^{2,5} Susumu Kitagawa^{1,2,6*}

Carbon monoxide (CO) produced in many large-scale industrial oxidation processes is difficult to separate from nitrogen (N₂), and afterward, CO is further oxidized to carbon dioxide. Here, we report a soft nanoporous crystalline material that selectively adsorbs CO with adaptable pores, and we present crystallographic evidence that CO molecules can coordinate with copper(II) ions. The unprecedented high selectivity was achieved by the synergetic effect of the local interaction between CO and accessible metal sites and a global transformation of the framework. This transformable crystalline material realized the separation of CO from mixtures with N₂, a gas that is the most competitive to CO. The dynamic and efficient molecular trapping and releasing system is reminiscent of sophisticated biological systems such as heme proteins.

Carbon monoxide (CO) is a central resource for carbon-based chemical products such as polymer fibers, plastics, and medicines (1–4). Although huge amounts of CO are produced in industrial processes such as steel manufacturing, CO is mixed with other gases (such as unburned N₂ from air). This exhaust gas cannot be used as a carbon resource and is burned to produce a huge amount of CO₂. For effective separation, the selective uptake and ready release of CO are inseparable; however, these objectives often conflict because the trade-off for the increase in interaction with CO is some loss of ease in subsequent CO release. To date, CO separation has been limited to processes that strongly chemisorb CO on transition metal ions such as mono-

valent Cu⁺ (5), but high temperatures are required to release CO. A synergistic system that makes use of a weak local interaction and subsequent global structural change could overcome this limitation in a manner similar to allosteric effects in the binding and release of O₂ by heme proteins (6).

Despite their crystalline form, porous coordination polymers (PCPs) or metal-organic frameworks (7–10) can provide a nanometer-sized soft space that is transformable in response to guest accommodation (11–17). This feature encouraged us to create a synergy system in a PCP solid to achieve the ultimate separation of mixed gases. Herein, we report on a PCP that has specific but weak CO adsorption and recognition sites and a reversibly transformable framework. Weak adsorption of CO on the Cu²⁺ site induces marked global structural changes in a positive cooperative manner, which produces additional space and allows further adsorption of CO as so-called reversible self-accelerating CO adsorption (fig. S1 and movie S1) (18). As a result, this crystalline porous compound achieved unprecedented highly effective trapping of CO from a gas mixture with N₂.

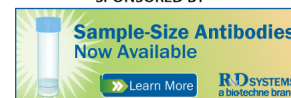
We prepared the PCP 1 composed of 5-azidoisophthalate (aip) (19) and divalent Cu²⁺

ions. In the as-synthesized crystal of PCP 1 {[Cu(aip)(H₂O)](solvent)_n} (where *n* is the number of solvent molecules), the Cu²⁺ and aip ligands form Cu²⁺ paddle-wheel units, the axial positions of which are occupied by water molecules (Fig. 1A). An infinite kagomé-type two-dimensional (2D) sheet structure (20, 21) is formed through the connection between the paddle-wheel units by the aip ligands (Fig. 1B). The 2D sheets are stacked with a separation distance of 6.7 Å, creating two types of 1D infinite channels with cross-section sizes of 9 × 9 Å² (channel *L*; hexagonal larger channel) and 4 × 4 Å² (channel *S*; triangular smaller channel), respectively, along the *c* axis (Fig. 1, B to D). The total solvent-accessible volume was estimated to be 38% (766 Å³) of the unit cell volume. The contributions by channels *L* and *S* to the total solvent-accessible volume were estimated as 65% (498 Å³) and 35% (268 Å³), respectively.

Thermogravimetric analysis (fig. S2) (18) indicated that the guest molecules were easily removed by heating at 80°C to give a dried PCP 2 [Cu(aip)] that is thermally stable up to ~180°C. We determined the crystal structure of the dried PCP 2 by Rietveld analysis using synchrotron powder x-ray diffraction data (fig. S3) (18). The removal of water molecules from the axial site of the Cu²⁺ paddle-wheel unit caused one of the carboxylate oxygen atoms in the adjacent layer to coordinate to this site to form the paddle-wheel chains along the *c* axis (Fig. 1, E and H, and fig. S5) (18). We observed marked changes in the shape and volume of channels upon the removal of the guest molecules (Fig. 1, F and G). The total solvent-accessible volume was reduced from 38% of the unit cell to 25%. In the structure of the dried PCP 2, the carboxylates twisted against the Cu–Cu axis, and the aromatic planes further inclined to the pores to make the channels narrower than those of the as-synthesized PCP 1. We noted distinct shape changes in channel *S*. Channel *S* was squeezed at the neck, causing a structural change from a bellows-like shape (Fig. 1C) to a garlic-like shape (Fig. 1G) (each pore is almost separated). We expected that access of

¹Institute for Integrated Cell-Material Sciences (WPI-iCeMS), Kyoto University, Kyoto 615-8510, Japan. ²RIKEN Spring-8 Center, Hyogo 679-5148, Japan. ³Fukui Institute for Fundamental Chemistry, Kyoto University, Kyoto 606-8103, Japan. ⁴Institute for Materials Research, Tohoku University, Sendai 980-8577, Japan. ⁵Japan Synchrotron Radiation Research Institute/Spring-8, Hyogo 679-5198, Japan. ⁶Department of Synthetic Chemistry and Biological Chemistry, Graduate School of Engineering, Kyoto University, Kyoto 615-8510, Japan.

*Corresponding author. E-mail: rmatsuda@icems.kyoto-u.ac.jp (R.M.); kitagawa@icems.kyoto-u.ac.jp (S.K.)



www.rndsystems.com



Heteroepitaxial Growth of Two-Dimensional Hexagonal Boron Nitride Templated by Graphene Edges

Lei Liu *et al.*

Science **343**, 163 (2014);

DOI: 10.1126/science.1246137

This copy is for your personal, non-commercial use only.

If you wish to distribute this article to others, you can order high-quality copies for your colleagues, clients, or customers by [clicking here](#).

Permission to republish or repurpose articles or portions of articles can be obtained by following the guidelines [here](#).

The following resources related to this article are available online at www.sciencemag.org (this information is current as of March 25, 2016):

Updated information and services, including high-resolution figures, can be found in the online version of this article at:

</content/343/6167/163.full.html>

Supporting Online Material can be found at:

</content/suppl/2014/01/09/343.6167.163.DC1.html>

This article **cites 23 articles**, 1 of which can be accessed free:

</content/343/6167/163.full.html#ref-list-1>

This article has been **cited by** 2 articles hosted by HighWire Press; see:

</content/343/6167/163.full.html#related-urls>

This article appears in the following **subject collections**:

Materials Science

/cgi/collection/mat_sci